Energy & Environmental Science

Cite this: *Energy Environ. Sci.*, 2012, **5**, 9121

www.rsc.org/ees

PAPER

Thermoelectric properties of Sr_3GaSb_3 – a chain-forming Zintl compound

Alex Zevalkink,†*[a] Wolfgang G. Zeier,†[ab] Gregory Pomrehn,†[a] Eugen Schechtel,[a] Wolfgang Tremel[b] and G. Jeffrey Snyder[a]

Received 29th May 2012, Accepted 15th August 2012
DOI: 10.1039/c2ee22378c

Inspired by the promising thermoelectric properties in the Zintl compounds Ca_3AlSb_3 and $Ca_5Al_2Sb_6$, we investigate here the closely related compound Sr_3GaSb_3. Although the crystal structure of Sr_3GaSb_3 contains infinite chains of corner-linked tetrahedra, in common with Ca_3AlSb_3 and $Ca_5Al_2Sb_6$, it has twice as many atoms per unit cell ($N = 56$). This contributes to the exceptionally low lattice thermal conductivity ($\kappa_L = 0.45$ W m^{-1} K^{-1} at 1000 K) observed in Sr_3GaSb_3 samples synthesized for this study by ball milling followed by hot pressing. High temperature transport measurements reveal that Sr_3GaSb_3 is a nondegenerate semiconductor (consistent with Zintl charge-counting conventions) with relatively high p-type electronic mobility (~30 cm^2 V^{-1} s^{-1} at 300 K). Density functional calculations yield a band gap of ~0.75 eV and predict a light valence band edge (~0.5 m_e), in qualitative agreement with experiment. To rationally optimize the electronic transport properties of Sr_3GaSb_3 in accordance with a single band model, doping with Zn^{2+} on the Ga^{3+} site was used to increase the p-type carrier concentration. In optimally hole-doped $Sr_3Ga_{1-x}Zn_xSb_3$ ($x = 0.0$ to 0.1), we demonstrate a maximum figure of merit of greater than 0.9 at 1000 K.

Introduction

Thermoelectric materials, which allow for solid-state conversion of heat into electricity, have the potential to reduce the huge quantity of energy currently lost in the form of waste heat. However, to make widespread implementation practicable, improvements to the efficiency of thermoelectric materials are necessary.[1,2] Thermoelectric efficiency is a function of the figure of merit of a material, given by $zT = \alpha^2 T/\rho\kappa$, where α is the Seebeck coefficient, ρ is electrical resistivity, and κ is the thermal conductivity. Most easily achieved in heavily doped semiconductors, a careful balance must be obtained between these often conflicting and highly interdependent material properties.[3]

Zintl compounds, characterized by covalently bonded "substructures", surrounded by highly electropositive cations, have recently attracted attention due to their often complex crystal structures.[4,5] In general, the lattice thermal conductivity of Zintl compounds trends with unit cell complexity;[6,7] $Yb_{14}AlSb_{11}$, containing 104 atoms per unit cell, exhibits one of the lowest known lattice thermal conductivities of any bulk material.[8] In contrast, the electronic mobility in Zintl compounds is more difficult to predict, though the nature of the covalently bonded substructure is thought to play a major role. For

[a]*Materials Science, California Institute of Technology, 1200 E. California Blvd., Pasadena, CA 91125, USA*
[b]*Institute for Inorganic Chemistry and Analytical Chemistry, University of Mainz, Duesbergweg 10-14, D-55099 Mainz, Germany*
† All the authors contributed equally to this manuscript.

Broader context

Thermoelectric materials have the potential to reduce the huge quantity of energy currently lost in the form of waste heat. However, to make widespread implementation possible, improvements to both the efficiency and toxicity of thermoelectric materials are necessary. Inspired by promising thermoelectric properties in the relatively inexpensive and earth-abundant compounds Ca_3AlSb_3 and $Ca_5Al_2Sb_6$, this study investigates the closely related Zintl compound Sr_3GaSb_3. We report on the electronic and thermal transport properties of Sr_3GaSb_3 and show that these properties can be controlled by substituting Zn^{2+} on the Ga^{3+} site to increase the p-type carrier concentration and ultimately optimize the thermoelectric properties. Compared to previously studied Ca_3AlSb_3 and $Ca_5Al_2Sb_6$, the larger unit cell and increased density of Sr_3GaSb_3 leads to an extremely low lattice thermal conductivity (0.45 W mK^{-1} at 1000 K). This, combined with optimization of the electronic properties through doping, leads to a peak figure of merit (zT) of 0.94 at high temperatures. This is a significant improvement over previously studied chain-forming Zintl compounds, arising from the improved power factor and significantly reduced thermal conductivity.

example, a relatively high electronic mobility has been demonstrated in AM_2Sb_2 (A = alkaline or rare earth, M = transition metal) compounds, which form 2-dimensional covalent planes ($\mu \sim 100$ cm^2 V^{-1} s^{-1}),[9–11] while $Yb_{14}AlSb_{11}$, characterized by isolated $AlSb_4$ tetrahedra and Sb_3 moieties exhibits extremely low carrier mobility ($\sim$5 cm^2 V^{-1} s^{-1}).[8] This is not true in all cases however; despite being highly covalent, 3-dimensional anionic structures, the clathrate compounds generally do not exhibit high carrier mobility, due to disorder in the anionic sites.[12,13]

Bridging these well-characterized 3-, 2-, and 0-dimensional structures are the relatively little-known 1-dimensional, chain-forming Zintl compounds. We have recently reported on the thermoelectric properties of Ca_3AlSb_3 and $Ca_5Al_2Sb_6$,[14,15] each of which forms a distinct structure characterized by infinite, parallel chains of corner-sharing $AlSb_4$ tetrahedra, shown in Fig. 1b and c.[16,17] The large, complex unit cells of Ca_3AlSb_3 and $Ca_5Al_2Sb_6$ (28 and 26 atoms per cell, respectively) lead to low lattice thermal conductivities (<0.6 W m^{-1} K^{-1} at 1000 K). Upon carrier concentration optimization, promising figures of merit have been obtained (0.78 and 0.6 at 1000 K, respectively). Further improvements to zT in this class of compounds might be achieved by further reducing the acoustic contribution to the lattice thermal conductivity ($\kappa_{acoustic}$), given by eqn (1) in the limit of Umklapp scattering.

$$\kappa_{acoustic} = \frac{(6\pi^2)^{2/3}}{4\pi^2} \frac{\bar{M} v_s^3}{TV^{2/3}\gamma^2} \frac{1}{N^{1/3}} \quad (1)$$

Here, $\bar{M}$ and V are average atomic mass and atomic volume, respectively, v_s is the average speed of sound, γ is the Grüneisen parameter, and N is the number of atoms per unit cell.[6] Since $v_s \propto \sqrt{E}/\sqrt{d}$, where E is the stiffness and d is the density, heavy atoms and soft bonds lead to low v_s and thus low κ_L. This motivates our current study of the compound Sr_3GaSb_3, which has not been previously investigated for thermoelectric applications.[18] While Sr_3GaSb_3 is a chain-forming compound similar to Ca_3AlSb_3 and $Ca_5Al_2Sb_6$ (see Fig. 1a), it has twice as many atoms per unit cell ($N = 56$) and significantly higher density. Additionally, our previous study of the $Ca_5M_2Sb_6$ system suggests that M = Ga leads to a greater degree of covalent bonding in the anionic sub-structure than M = Al, which leads in turn to a lighter band mass and higher mobility, further motivating the current study.[19,20]

Sr_3GaSb_3 is the only compound known to crystallize in a unique, chain-based structure that, according to Schäfer *et al.*, can be considered a connecting link between the structures based on either linear chains or isolated tetrahedra-pairs formed by all other known A_3MPn_3 compounds (A = Ca, Sr, Ba, M = Al, Ga, In, and Pn = P, As, Sb).[18] The monoclinic structure of Sr_3GaSb_3 (space group $P2_1/n$, lattice parameters $a = 11.855$ Å, $b = 14.649$ Å, $c = 11.876$ Å, and β angle = 109.963°) contains infinite, closely packed, non-linear chains of corner sharing tetrahedra, characterized by four-tetrahedra repeat units, as shown in Fig. 2a. This four-tetrahedra periodicity in Sr_3GaSb_3 leads to a larger unit cell than that of Ca_3AlSb_3, which has a single-tetrahedron periodicity. The chains in Sr_3GaSb_3 are aligned along the [101] direction, shown pointing into the page in Fig. 2b. A single chain is highlighted in red. Note that while the chains appear to overlap with nearby chains to form zigzagging planes, staggering along the [101] direction prevents strong interactions between neighboring chains.

Here we use high temperature thermal and electronic transport measurements to characterize the thermoelectric properties of Sr_3GaSb_3. Doping with Zn^{2+} on the Ga^{3+} site is used to optimize the electronic properties according to a single band model. In addition, we have employed electronic structure calculations to shed light on the role of bonding in the electronic transport properties of Sr_3GaSb_3, potentially contributing to the development of guiding structure–property relationships for ternary Zintl thermoelectrics.

Experimental

Bulk, polycrystalline $Sr_3Ga_{1-x}Zn_xSb_3$ samples with compositions $x = 0.00$, 0.02, 0.05, 0.07, and 0.1 were prepared by ball milling followed by hot pressing, starting with elemental Sr, Zn, Sb, and GaSb. A GaSb precursor was synthesized from Ga (99.99% shot, Sigma-Aldrich) and Sb (99.9999%, shot, Alfa Aesar) in an evacuated quartz ampoule which was held at 1000 K for 12 hours followed by water-quenching. The elements (99%

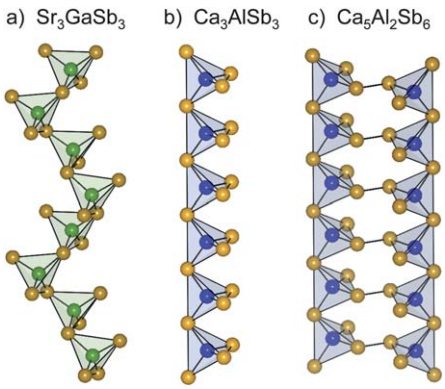

Fig. 1 The distinct chain-like polyanions formed by the Zintl antimonides Sr_3GaSb_3, Ca_3AlSb_3 and $Ca_5Al_2Sb_6$. Sb (orange) resides at the tetrahedral corners, while either Ga (green) or Al (blue) resides in the centers.

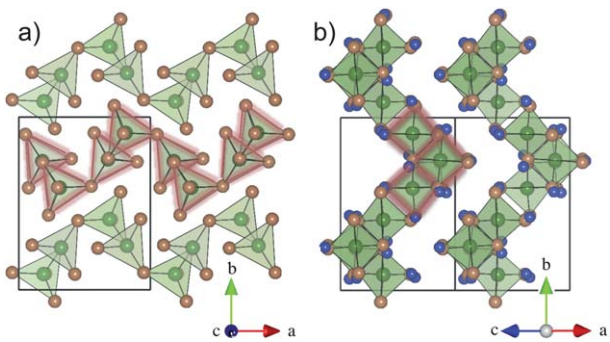

Fig. 2 a) Sr_3GaSb_3 contains unique chains of corner-sharing $GaSb_4$ tetrahedra, formed from four-tetrahedra repeat units. Ga atoms are green, those of Sb are orange, and Sr atoms are not shown. (b) The structure of Sr_3GaSb_3 viewed down the [101] axis, with chains going into the page (Sr atoms shown in blue). In both orientations, a single chain is highlighted in red.

pieces Sr, 99.99% Zn shot, and 99.9999% Sb shot from Alfa Aesar) were cut into small pieces and loaded with the GaSb precursor in stoichiometric amounts into stainless-steel vials, with stainless-steel balls in an Ar dry box. The mixtures were milled for 90 min using an SPEX Sample Prep 8000 Series Mixer/Mill. The resulting powder was consolidated by induction hot pressing in high density graphite dies from POCO. The die was heated to 873 K in 2 hours and held for 1.5 hours, followed by a 30 min ramp to 973 K, at which point a pressure of 120 MPa was applied. These conditions were maintained for 2 hours, followed by a 2 hour pressure-free cool down. The resulting ingots, which were sensitive to air and moisture, were sliced into disks for characterization.

X-ray diffraction measurements were carried out on a Philips PANalytical X'Pert Pro with CuKα radiation. Pawley refinements were performed using TOPAS Academic V4.1,[21] applying the fundamental parameter approach using the crystallographic data from Cordier *et al.*[18] Scanning electron microscopy (SEM) and energy-dispersive X-ray spectroscopy (EDS) of the consolidated material were performed using a Zeiss 1550 VP SEM. The samples used in the measurements of thermal diffusivity, Seebeck coefficient and Hall coefficient were disks (cut perpendicular to the pressing direction) 12 mm in diameter, and approximately 1 mm thick. Furthermore, for comparison, slices were cut parallel to the hot pressing direction, to test for anisotropic transport properties. Thermal diffusivity was measured using a Netzsch laser flash diffusivity instrument (LFA 457) with samples coated in a thin layer of graphite to minimize errors in the emissivity. The data were analyzed using a Cowan model with pulse correction. Heat capacity (C_p) was estimated using the method of Dulong–Petit. The Seebeck coefficient was calculated from the slope of the thermopower *vs.* temperature gradient measurements from chromel-Nb thermocouples.[22] Electrical resistivity and Hall coefficients were measured using the van der Pauw technique under a reversible magnetic field of 1 T using pressure-assisted contacts. All measurements were carried out during both heating and cooling cycles, and for samples with high zT, each measurement was repeated for further verification. There was no hysteresis found between heating and cooling, nor between subsequent measurements. The combined uncertainty for all measurements involved in zT determination is ~20%.

Density functional calculations were performed with the WIEN2K code[23] based on the full-potential linearized augmented plane-wave (FP-LAPW) method under the generalized gradient approximation (GGA) as parameterized by Perdew, Burke, and Ernzerhof (PBE).[24] A plane wave basis cutoff of $R_{mt}K_{max} = 9$ was used in terms of the smallest muffin tin radius and maximum plane wave vector respectively. Muffin tin radii were 2.4 a.u. for Sr and 2.5 a.u. for both Ga and Sb. Calculations were performed at the theoretical ground state lattice parameters as determined by structural minimization of the unit cell. Atomic positions were relaxed to converged forces below 0.025 eV Å^{-1} on each atom. Total energy convergence was achieved in the self-consistent calculations with a shifted 6 × 4 × 6 k-point mesh, which reduced to 36 symmetrically unique k-points. The modified Becke–Johnson (TB-mBJ)[25] semi-local exchange potential was employed, which has been shown to improve the band gap in sp bonded semiconductors.[26] This method was used to produce the density of states and electronic dispersions shown in this work.

Results and discussion

Following ball milling and hot pressing, the polycrystalline $Sr_3Ga_{1-x}Zn_xSb_3$ (x = 0, 0.02, 0.05, and 0.07) samples had geometric densities that were ~98% of the theoretical density. SEM analysis using backscattered electrons reveals small, light-colored precipitates (see upper left panel of Fig. 3), identified by EDS as the Zintl phase Sr_2Sb_3. This phase appears to comprise approximately 1–3 vol% of each sample. X-ray diffraction confirms that Sr_3GaSb_3 and Sr_2Sb_3 were the only phases present in samples with $x = 0.0$ to 0.07 (shown in Fig. 3). The inset shows a magnified view in which the most prominent Sr_2Sb_3 peaks are marked with asterisks. The fraction of this phase was comparable in each of the samples with $x = 0.0$ to 0.07. In the sample with the nominal composition, $Sr_3Ga_{0.9}Zn_{0.1}Sb_3$, additional phases were present, including $SrZn_2Sb_2$, indicating that the solubility limit of Zn in Sr_3GaSb_3 was exceeded. We have therefore not included the transport properties of this composition. In all samples, the grain size after hot pressing was extremely small, estimated from fracture surfaces to be in the sub-micrometer range (upper right

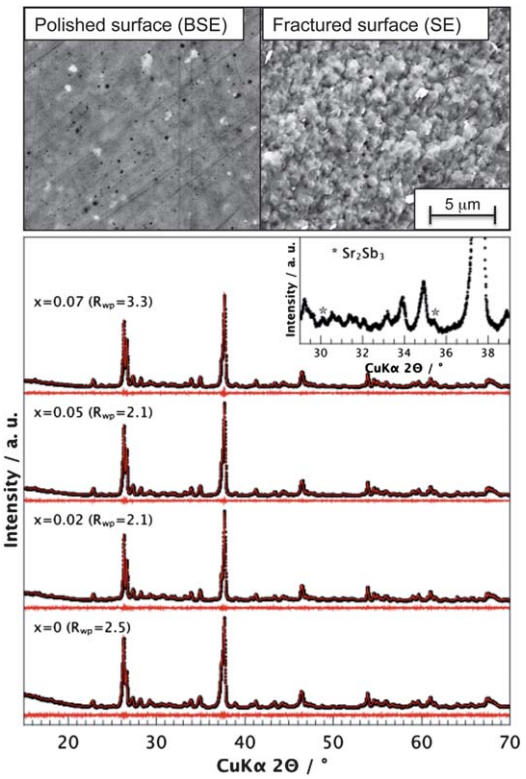

Fig. 3 Top: back-scattered electron image of a polished Sr_3GaSb_3 sample reveals the secondary phase Sr_2Sb_3 as white specks, while secondary electron imaging of a fracture surface shows the very small grain size (<1 µm). Bottom: X-ray diffraction data for $Sr_3Ga_{1-x}Zn_xSb_3$ including profile fit, profile difference, and profile residuals from the corresponding Pawley refinement including the secondary phase Sr_2Sb_3. The inset shows the reflections indexed to the impurity phase marked by asterisks.

panel in Fig. 3), in accordance with the broad profiles of the XRD reflections. No obvious texturing was seen in the diffraction patterns, despite the anisotropic crystal structure.

Electronic structure

Sr_3GaSb_3 forms a valence precise crystal structure that can be described within the Zintl formalism as follows: the highly electropositive Sr (3 Sr^{2+}) atoms donate their valence electrons to the anionic chains. Two of the Sb atoms making up the chains have only one covalent bond, leading to a valence state of −2, while one Sb atom is shared between two tetrahedra, leading to two covalent bonds and a valence state of −1. Assigning a valence state of −1 to the four-bonded Ga leads to overall charge balance and the formation of the covalent anionic chains.[27]

The basic features of this simple bonding description are reflected in the calculated density of states, shown in Fig. 4a. The prominent Ga and Sb electronic states deep in the valence band (−4 to −6 eV) and at the conduction band minimum likely correspond to Ga–Sb bonding and anti-bonding interactions, respectively. The valence band maximum is dominated by Sb states, likely arising from non-bonding Sb lone-pairs. In contrast, the conduction band is formed primarily by Ga–Sb anti-bonding states and by Sr states at higher energies, consistent with the assumption that Sr donates its valence electrons to form the anionic substructure. A band gap of ∼0.75 eV is predicted, qualitatively consistent with the experimentally observed behavior described below.

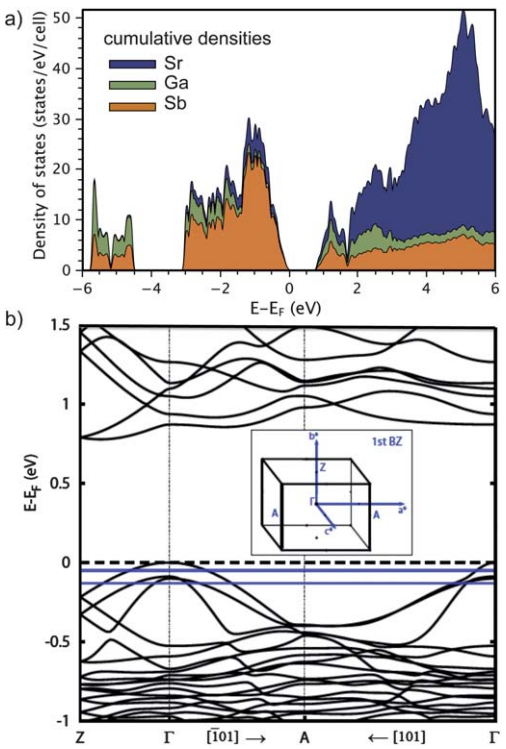

Fig. 4 a) Density of states and (b) the band structure of Sr_3GaSb_3 reveal an indirect band gap of ∼0.75 eV. The upper and lower blue lines correspond to carrier concentrations of 10^{19} and 10^{20} holes per cm^3, respectively. Inset: Brillouin zone of Sr_3GaSb_3 with selected k-space directions labeled.

The electronic band structure of Sr_3GaSb_3 is shown in Fig. 4b in the k-space direction parallel to the $GaSb_4$ chains (Γ–$A_{[101]}$), and in the two perpendicular directions (Γ–Z and Γ–$A_{[\bar{1}01]}$). The k-space points Γ, A and Z are labeled in the Brillouin zone shown in the inset. The band structure is characterized by an indirect band gap (∼0.75 eV) with the valence band maximum at Γ and the conduction band minimum between Γ and Z. The upper and lower blue lines correspond to carrier concentrations of 10^{19} and 10^{20} holes per cm^3, respectively. At energies very close to the valence band maximum (0 to −0.1 eV), the dispersion is anisotropic, with the effective mass along the chains ($m^*_{[101]} = 0.18\ m_e$) smaller than the mass in the perpendicular directions ($m^*_{[\bar{1}01]} = 0.57\ m_e$ and $m^*_{[010]} = 0.66\ m_e$). In contrast, the two additional bands with maxima at ∼−0.1 eV are nearly isotropic. When electrons are scattered primarily by acoustic phonons, as is the case in most known thermoelectric materials, the improvement in carrier mobility conferred by a light band mass outweighs the detrimental effect that low m^* has on α. In this case, the thermoelectric quality factor is given by $\beta \propto \frac{N_v}{m_i^* \kappa_L}$, where m_i^* is the mass of a single hole pocket along the conduction direction.[20,28,29] This suggests that the light band mass in Sr_3GaSb_3, particularly in the direction of the chain substructures ($m^*_{[101]}$), may be advantageous.

The number of bands contributing to transport (N_v) at a given carrier concentration influences the figure of merit of a material, as illustrated by the thermoelectric quality factor. If N_v is high, it is possible to simultaneously have light bands (small m_i^*) and large density of states effective mass. In Sr_3GaSb_3, only one band contributes to transport at energies very close to the valence band maximum. In heavily doped Sr_3GaSb_3 ($n > 10^{20}$ holes per cm^3), the contribution from the two bands with maxima at about −0.1 eV could potentially lead to $N_v = 3$.

Electronic transport properties

Fig. 5b shows the measured Hall carrier concentrations (n_H) of $Sr_3Ga_{1-x}Zn_xSb_3$ samples as a function of temperature. Despite Sr_3GaSb_3 being a valence-precise Zintl compound, the undoped material has an extrinsic p-type carrier concentration of 4×10^{18} holes per cm^3 at room temperature, most likely due to intrinsic defects in the crystal structure. The resistivity of undoped Sr_3GaSb_3 is very high (Fig. 5a), decreasing due to thermal activation of carriers into the conduction band above 800 K.

With each substitution of Zn^{2+} on a Ga^{3+} site we expect to introduce one additional free hole (h^+), due to the difference in valence states.[4] In many Zintl compounds, this simple assumption works well for predicting n_H of doped samples (*i.e.* $Yb_{14}Al_{1-x}Mn_xSb_{11}$, $Ba_8Ga_{16-x}Ge_{30+x}$[8,12]), indicating that the dopant primarily substitutes on the intended crystallographic sites. However, in the case of Sr_3GaSb_3, in common with Ca_3AlSb_3,[31] doping with Zn results in only a fraction of the predicted hole concentration. For example, when $x = 0.07$ (equivalent to a synthetic concentration of 1 at% Zn) we would predict $n = 2.1 \times 10^{20}\ h^+\ cm^{-3}$. However, the measured n_H is only $5 \times 10^{19}\ h^+\ cm^{-3}$. If each measured hole is assumed to result from a Zn atom on a Ga site, then only *one-fourth* of the synthetic Zn content resides on the intended site, while the remainder may form secondary phases too small to identify or perhaps becomes

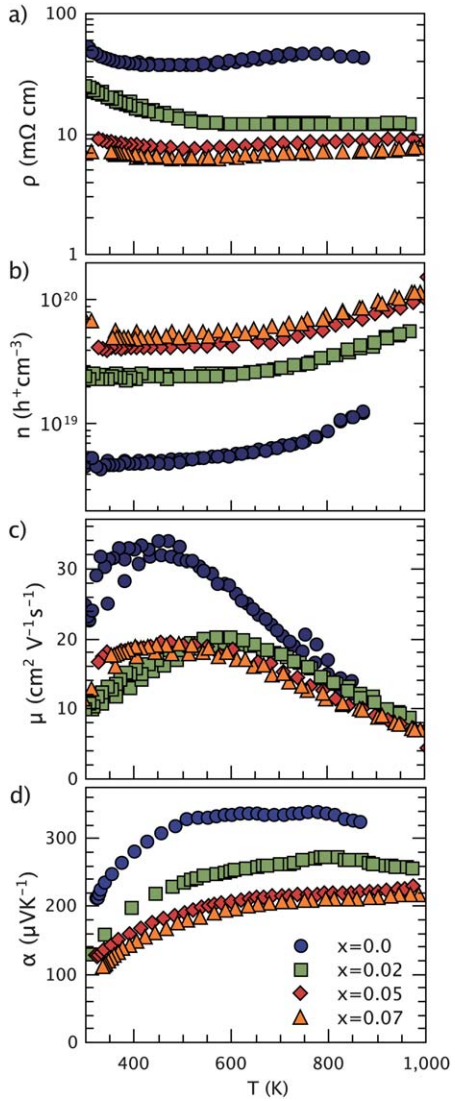

Fig. 5 The temperature dependence of (a) the electrical resistivity, ρ, and (b) the Hall carrier concentration, n_H, in $Sr_3Ga_{1-x}Zn_xSb_3$ illustrates the transition towards degenerate semiconducting behavior upon Zn doping. (c) The Hall mobility, μ_H, reveals activated behavior at low temperature and (d) the Seebeck coefficient, α, becomes more metallic with increasing Zn.

trapped at grain boundaries. However, estimating the matrix Zn content from the measured Hall coefficient can be misleading. Sources of error might include Zn defects with an effective charge other than +1, formation of compensating n-type defects,[32] or a Hall factor ($r_H = n/n_H$) that deviates significantly from unity.

As a function of temperature, n_H in $Sr_3Ga_{1-x}Zn_xSb_3$ is constant at low temperatures, indicative of extrinsic transport, and increases at high temperature as intrinsic carriers are activated across the band gap. The increase in n_H leads to the decrease in electrical resistivity with Zn-doping as shown in Fig. 5a.

The Hall mobility, μ_H, is shown in Fig. 5c, calculated from $\rho = 1/n_H e\mu_H$. At low temperatures ($T < 500$ K), μ_H exhibits a positive temperature dependence that can be fit using $\mu_H \propto e^{-E_A/k_BT}$, where E_A is the activation energy associated with a potential barrier.[30] Such behavior may arise from barriers at the grain boundaries, such as oxide layers or secondary phases, requiring an activation energy to overcome. Our previous study of Ca_3AlSb_3 indicates that with the correct processing it is possible to avoid this activated behavior, drastically increasing electrical conductivity.[31] At higher temperatures (>600 K) the mobility in $Sr_3Ga_{1-x}Zn_xSb_3$ is limited by acoustic phonon scattering, for which the temperature dependence is given by $\mu_H \propto T^{-\nu}$, with ν between 1 and 1.5 for degenerate and non-degenerate behavior, respectively.[33]

The Seebeck coefficients, α, of the $Sr_3Ga_{1-x}Zn_xSb_3$ samples shown in Fig. 5d are positive, consistent with the p-type carrier concentrations. The Seebeck coefficient of undoped Sr_3GaSb_3 increases up to a temperature of 700 K, at which point thermally activated electrons result in a decay of α. From the resulting maximum ($\alpha_{max} \sim 340$ μV K^{-1}, $T_{max} \sim 700$ K), a rough estimate of the band gap using $E_g = 2e\alpha_{max}T_{max}$[34] yields $E_g \sim 0.5$ eV, which is in general agreement with the results of the DFT calculations (see Fig. 4). As expected, the Seebeck coefficients decrease with increasing carrier concentrations. This is best illustrated by the Pisarenko relation shown in the left panel of Fig. 7a), with experimental α and n_H (diamond symbols) obtained at 700 K. The solid curve was generated using the single parabolic band (SPB) model described in ref. 15 with a valence band effective mass of $m^* = 0.9$ m$_e$. All of the doped samples in this study appear to be well described by $m_e = 0.9\ m^*$ at 700 K, suggesting that, within experimental uncertainty, it is not possible to see any evidence of multi-band behavior at these doping levels. Although not shown here, the same effective mass also provides a good fit for the experimental Seebeck coefficients at 300 K and 500 K.

To investigate the possibility of anisotropic transport properties, the Hall and Seebeck coefficients of $Sr_3Ga_{0.93}Zn_{0.07}Sb_3$ were measured on disks cut in different directions (perpendicular and parallel to the hot pressing direction). An ~5% disparity in resistivity measured to 1000 K appeared to stem from a higher hole concentration in the perpendicular slice, while the mobility was identical in both directions. The difference in the Seebeck coefficients at 300 K was within the measurement uncertainty of 5%. Together, these results suggest that the anisotropy of Sr_3GaSb_3 does not significantly influence transport properties in our polycrystalline samples. This is in agreement with XRD measurements, which show no signs of preferred grain orientation (Fig. 3).

Thermal transport properties

The thermal conductivity (κ), shown in Fig. 6a was calculated from thermal diffusivity (D) using $\kappa = DdC_p$ (here, d = geometric density and C_p = Dulong Petit heat capacity, 0.250 J g^{-1} K^{-1}). While generally accurate at room temperature, the Dulong Petit heat capacity often underestimates C_p at high temperature by as much as 10–20%, leading to an overestimation of zT. The electronic contribution to the thermal conductivity (κ_e) was estimated using the Wiedemann–Franz relation $\kappa_e = LT/\rho$, where the Lorenz number, L, was determined from experimental Seebeck coefficients using an SPB model (inset of Fig. 6).[12] Subtracting κ_e from κ leaves the combined lattice (κ_L) and bipolar (κ_B) contributions shown in Fig. 6b). Of the samples in this study, only undoped Sr_3GaSb_3 exhibits a significant bipolar contribution,

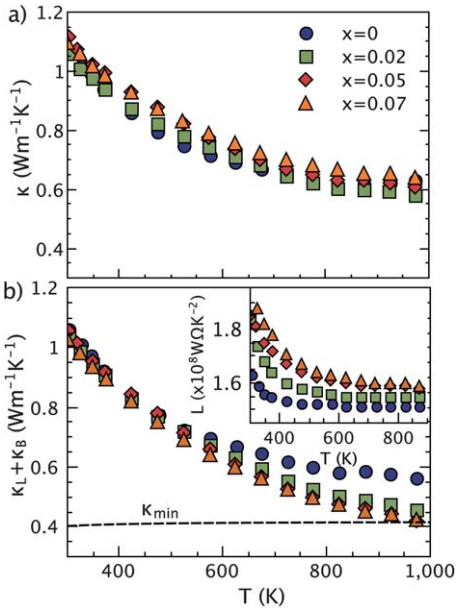

Fig. 6 a) Total thermal conductivity and (b) lattice thermal conductivity of $Sr_3Ga_{1-x}Zn_xSb_3$. The calculated minimum lattice thermal conductivity κ_{min} is shown as a broken line, and the inset shows the calculated Lorenz numbers generated using an SPB model.[12]

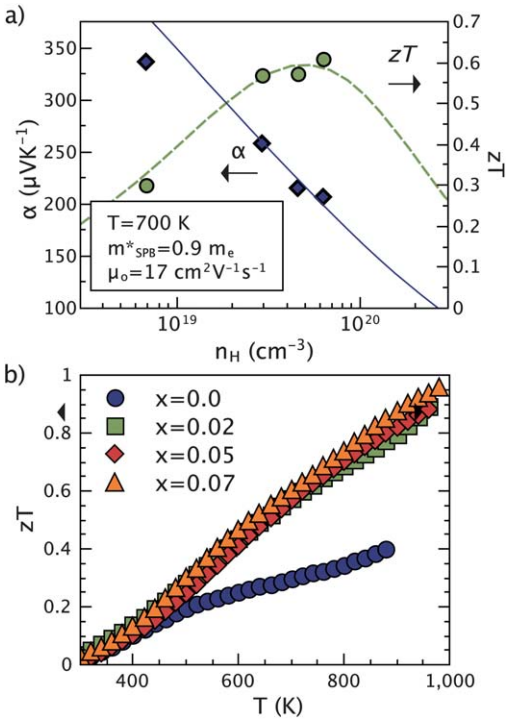

Fig. 7 a) Seebeck coefficients (diamonds) and zT (circles) vary with carrier concentration approximately according to an SPB model at 700 K. The solid and broken curves represent the predicted SPB behavior of α and zT, respectively, assuming $m^* = 0.9\ m_e$, $\mu_0 = 17\ cm^2\ V^{-1}\ s^{-1}$ and $\kappa_L = 0.55\ W\ m^{-1}\ K^{-1}$ (see Table 1). (b) The measured figure of merit of $Sr_3Ga_{1-x}Zn_xSb_3$ exceeds 0.9 when heavily doped.

evidenced by the increase in $\kappa_L + \kappa_B$ at high temperatures relative to the doped samples.[38] In the remaining compositions ($x = 0.02$, 0.05, 0.07), the lattice thermal conductivity is the dominant term, decreasing with the $1/T$ temperature dependence expected when scattering is dominated by Umklapp processes (eqn (1)).[6]

The large number of atoms per unit cell in Sr_3GaSb_3 ($N = 56$), leads, by definition, to a phonon dispersion with 3 acoustic modes and 55 × 3 optical modes. Such complexity in the dispersion leads to both enhanced Umklapp scattering and flattened, low velocity optical modes that contribute very little to heat transport.[6,7] These features, combined with the small grain size in our Sr_3GaSb_3 samples, lead to the extremely low lattice thermal conductivity observed in this material. To estimate the minimum lattice thermal conductivity, κ_{min}, for Sr_3GaSb_3, and thus to determine whether further nanostructuring would be beneficial, we have employed Cahill's formula for disordered crystals.[35,36] κ_{min} is dependent on the longitudinal and transverse sound velocities, which were determined from ultrasonic measurements to be 3750 m s^{-1} and 2130 m s^{-1}, respectively. These yield an estimated Debye temperature of $\theta_D = 243$ K and $\kappa_{min} = 0.43\ W\ m^{-1}\ K^{-1}$. At high temperatures, the lattice thermal conductivity of Sr_3GaSb_3 approaches the estimated κ_{min}, in common with Ca_3AlSb_3 and $Ca_5Al_2Sb_6$, adding to the growing body of evidence suggesting that large unit cell size leads to the glass-like high temperature κ_L observed in a number of thermoelectric materials.

Figure of merit

The figure of merit of $Sr_3Ga_{1-x}Zn_xSb_3$ is shown in Fig. 7b as a function of temperature. The transition from nondegenerate behavior to degenerate semiconducting behavior upon doping with zinc leads to an increase in the maximum zT from 0.4 for $x = 0$ to greater than 0.9 when $x = 0.07$. To provide a rough estimate of the optimal carrier concentration in this material we have employed an SPB model at 700 K (see Fig. 7a). At 700 K, it is reasonable to assume that extrinsic carriers still dominate transport and acoustic phonons are the primary scattering source. Using input parameters $m^* = 0.9\ m_e$, $\mu_0 = 17\ cm^2\ V^{-1}\ s^{-1}$ and $\kappa_L = 0.55\ W\ m^{-1}\ K^{-1}$, the predicted optimum carrier concentration is approximately $5 \times 10^{19}\ h^+\ cm^{-3}$. The doped samples in this study have carrier concentrations clustered around this optimum, explaining their similar zT values.

Relative to the previously studied chain-based Zintl compounds, $Ca_5Al_2Sb_6$ and Ca_3AlSb_3, Sr_3GaSb_3 exhibits a higher figure of merit across the entire measured temperature range. As discussed above, the maximum figure of merit in a given thermoelectric material is related to its quality factor, $\beta \propto \frac{N_v}{m_i^* \kappa_L}$. It is instructive to compare these fundamental material properties across closely related Zintl compounds. Here, we consider the three chain-forming Zintl antimonides, $Ca_5Al_2Sb_6$, Ca_3AlSb_3, and Sr_3GaSb_3. The distinct chain-based anionic structure of each compound is shown in Fig. 1.

The density of states effective mass of each compound (m^*), determined by fitting experimental Seebeck coefficients using a single band model,[14,15] are given in Table 1. The density of states effective mass is related to the average mass of individual hole pockets, m^*_{band}, by the expression $m^* = N_v^{2/3} m^*_{band}$. Note that m^*_{band} is directly related to the inertial mass, m_i^*. Since $N_v \sim 2$ in

Table 1 Experimental properties of chain forming Zintl antimonides[14,15] are given at 300 K unless otherwise specified. N_v is the approximate band degeneracy at optimal doping levels, m^* is the effective mass obtained by fitting an SPB model to the experimental Pisarenko relation, d is theoretical density, G and K are the shear and bulk moduli determined from the transverse and longitudinal sound velocities, v_T and v_L. From ref. 16–18, $\bar{M}$ and V are the average atomic mass and atomic volume, and N is the number of atoms per unit cell

	zT_{max} ~1000 K	N_v	m^* (m_e)	d (g cm^{-3})	G (GPa)	K (GPa)	v_T (m s^{-1})	v_L (m s^{-1})	M (amu)	V (Å^3)	Θ_D (K)	N
Sr_3GaSb_3	0.9	1–3	0.9	4.92	22.3	39.4	2130	3750	99.7	33.6	246	56
$Ca_5Al_2Sb_6$	0.6	2	2.2	4.31	24.8	39.4	2400	4100	75.8	29.2	286	26
Ca_3AlSb_3	0.75	2	0.8	4.14	24.6	39.1	2440	4170	73.2	29.4	292	28

each compound at optimal doping levels, the larger m^* in $Ca_5Al_2Sb_6$ derives almost entirely from its heavier m^*_{band}. This explains the low mobility of $Ca_5Al_2Sb_6$ samples ($\mu \propto m_i^{*}$), shown in the left panel of Fig 8. In contrast, both Ca_3AlSb_3 and Sr_3GaSb_3 have similar lighter m^* and thus relatively high hole mobilities. This is contrary to our expectation that Ga would lead to a lighter effective mass than that found in the Al-based compound. The difference in the mobility of these two compounds at low temperatures most likely stems from different degrees of processing-related deffects such as grain boundary oxidation or impurity phases, which lead to the activated temperature dependence. As discussed above, when acoustic phonons are the primary electron scattering source, the maximum zT in a given material is *inversely* proportional to the effective mass. It is likely, then, that the heavy effective mass of $Ca_5Al_2Sb_6$ contributes to its relatively low peak zT, compared with Ca_3AlSb_3 and Sr_3GaSb_3.

The improved peak zT of Sr_3GaSb_3 ($zT \sim 0.9$) compared with Ca_3AlSb_3 ($zT \sim 0.75$) can be attributed almost entirely to its lower κ_L. Shown in the right panel of Fig. 8 are the lattice thermal conductivities of each compound, estimated from the measured diffusivity of Zn-doped samples.[31,37] Though all three compounds exhibit an identical temperature dependence indicative of Umklapp scattering, κ_L in Sr_3GaSb_3 is about 25% lower across the entire temperature range. Accounting for traditional factors such as $\bar{M}$, V, and sound velocity (given in Table 1) explains only ~10% of the disparity, assuming that the Grüneisen parameter does not vary greatly between these three compounds (see eqn (1)). The remaining difference in κ_L can be explained by the exceptionally large unit cell of Sr_3GaSb_3 ($N = 56$), which is twice the size of $Ca_5Al_2Sb_6$ and Ca_3AlSb_3 and thus significantly reduces the acoustic lattice thermal conductivity (eqn (1)).

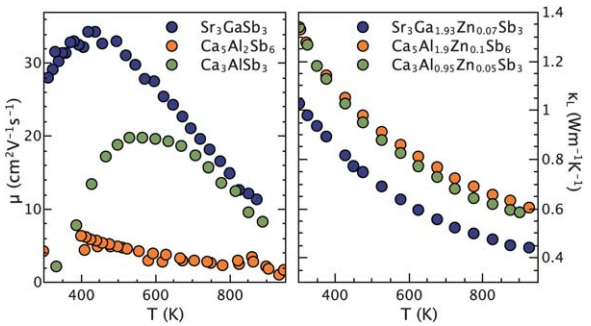

Fig. 8 Left: hole mobility of undoped $Ca_5Al_2Sb_6$, Ca_3AlSb_3, and Sr_3GaSb_3 samples. Right: lattice thermal conductivity of Zn-doped samples.[31,37]

Conclusion

Here, we have described a new thermoelectric material, Sr_3GaSb_3, which has a crystal structure characterized by chains of corner-linked tetrahedra, similar to the polyanions found in the previously studied Zintl compounds, $Ca_5Al_2Sb_6$ and Ca_3AlSb_3. In Sr_3GaSb_3, however, the chains are characterized by a repeating unit containing four tetrahedra, as opposed to the single tetrahedra repeat-unit found in $Ca_5Al_2Sb_6$ and Ca_3AlSb_3. The resulting large unit cell and comparatively high density in Sr_3GaSb_3 combine to yield the exceptionally low lattice thermal conductivity observed in this study ($\kappa_L = 0.45$ W m^{-1} K^{-1} at 1000 K). High temperature transport measurements reveal that Sr_3GaSb_3 is a nondegenerate p-type semiconductor, with a relatively large band gap ($E_g > 0.5$ eV) and high electronic mobility. Density functional calculations are in qualitative agreement, predicting a band gap of ~0.75 eV and a light valence band edge (~0.5 m_e). Doping with Zn^{2+} on the Ga^{3+} site leads to degenerate semiconducting behavior, allowing us to obtain p-type carrier concentrations near the optimum value predicted by a single parabolic band model. The combination of low lattice thermal conductivity, reasonable electronic mobility, and a sufficiently large band gap to maintain degenerate behavior at high temperature leads to a zT of 0.9 at 1000 K. Compared with previously studied chain-based Zintl compounds, both the peak zT and integrated zT of Zn-doped Sr_3GaSb_3 samples are significantly higher.

Acknowledgements

We gratefully acknowledge the NASA Jet Propulsion Laboratory for support. Wolfgang Zeier thanks the Carl-Zeiss foundation and acknowledges the funding through the Excellence Initiative (DFG/GSC 266).

References

1 L. Bell, Cooling, heating, generating power, and recovering waste heat with thermoelectric systems, *Science*, 2008, **321**, 1457–1461.
2 F. J. DiSalvo, Thermoelectric cooling and power generation, *Science*, 1999, **295**, 703.
3 G. J. Snyder and E. S. Toberer, Complex thermoelectric materials, *Nat. Mater.*, 2008, **7**, 105.
4 E. S. Toberer, A. F. May and G. J. Snyder, Zintl chemistry for designing high efficiency thermoelectric materials, *Chem. Mater.*, 2010, **22**, 624–634.
5 S. M. Kauzlarich, *Chemistry, Structure, and Bonding of Zintl Phases and Ions*, Wiley-VCH, 1996.
6 E. S. Toberer, A. Zevalkink and G. J. Snyder, Phonon engineering through crystal chemistry, *J. Mater. Chem.*, 2011, **21**, 15843–15852.
7 G. A. Slack, *Solid State Physics*, Academic Press, New York, 1979, vol. 34.

8 E. S. Toberer, C. A. Cox, S. R. Brown, T. Ikeda, A. F. May, S. M. Kauzlarich and G. J. Snyder, Traversing the metal-insulator transition in a Zintl phase: rational enhancement of thermoelectric efficiency in $Yb_{14}Al_xMn_{1-x}Sb_{11}$, *Adv. Funct. Mater.*, 2008, **18**, 2795.

9 E. S. Toberer, A. F. May, B. C. Melot, E. Flage-Larsen and G. J. Snyder, Electronic structure and transport in thermoelectric compounds AZn_2Sb_2 (A = Sr, Ca, Yb, Eu), *Dalton Trans.*, 2010, **39**, 1046–1054.

10 X.-J. Wang, M.-B. Tang, H.-H. Chen, X.-X. Yang, J.-T. Zhao, U. Burkhardt and Y. Grin, Synthesis and high thermoelectric efficiency of Zintl phase $YbCd_{2-x}Zn_xSb_2$, *Appl. Phys. Lett.*, 2009, **94**, 092106.

11 Q.-G. Cao, H. Zhang, M.-B. Tang, H.-H. Chen, X.-X. Yang, Y. Grin and J.-T. Zhao, Zintl phase $Yb_{1-x}Ca_xCd_2Sb_2$ with tunable thermoelectric properties induced by cation substitution, *J. Appl. Phys.*, 2010, **107**, 053714.

12 A. F. May, E. S. Toberer, A. Saramat and G. J. Snyder, Characterization and analysis of thermoelectric transport in n-type $Ba_8Ga_{16-x}Ge_{30-x}$, *Phys. Rev. B: Condens. Matter Mater. Phys.*, 2009, **80**, 125205.

13 B. C. Chakoumakos, B. C. Sales, D. G. Mandrus and G. S. Nolas, Structural disorder and thermal conductivity of the semiconducting clathrate $Sr_8Ga_{16}Ge_{30}$, *J. Alloys Compd.*, 2000, **296**, 80–86.

14 E. S. Toberer, A. Zevalkink, N. Crisosto and G. J. Snyder, The Zintl compound $Ca_5Al_2Sb_6$ for low-cost thermoelectric power generation, *Adv. Funct. Mater.*, 2010, **20**, 4375–4380.

15 A. Zevalkink, E. S. Toberer, W. Zeier, E. Flage-Larsen and G. J. Snyder, Ca_3AlSb_3: an inexpensive, non-toxic thermoelectric material for waste heat recovery, *Energy Environ. Sci.*, 2011, **4**, 510–518.

16 G. Cordier, E. Czech, M. Jakowski and H. Schaefer, Zintl phases of complex ions–information on $Ca_5Al_2Sb_6$ and $Ca_3Al_2As_4$, *Rev. Chim. Miner*, 1981, **18**, 9.

17 G. Cordier, H. Schaefer and M. Stelter, Ca_3AlSb_3 und $Ca_5Al_2Bi_6$ zwei neue Zintlphasen mit kettenfoermigen anionen, *Z. Naturforsch., B: Anorg. Chem., Org. Chem.*, 1984, **39**, 727–732.

18 G. Cordier, H. Schaefer and M. Stelter, Sr_3GaSb_3 und Sr_3InP_3, zwei neue Zintlphasen mit komplexen anionen, *Z. Naturforsch., B: Anorg. Chem., Org. Chem.*, 1987, **42**, 1268–1272.

19 A. Zevalkink, G. S. Pomrehn, S. Johnson, J. Swallow, Z. M. Gibbs and G. J. Snyder, Influence of the triel elements (M = Al, Ga, In) on the transport properties of $Ca_5M_2Sb_6$ Zintl compounds, *Chem. Mater.*, 2012, **24**(11), 2091–2098.

20 Y. Pei, A. D. Lalonde, H. Wang and G. J. Snyder, Low effective mass leading to high thermoelectric performance, *Energy Environ. Sci.*, 2012, **5**, 7963–7969.

21 A. Cohelo, TOPAS Academic V4.1, 2004.

22 S. Iwanaga, E. S. Toberer, A. Lalonde and G. J. Snyder, A high temperature apparatus for measurement of the Seebeck coefficient, *Rev. Sci. Instrum.*, 2011, **82**, 063905.

23 P. Blaha, K. Schwarz, G. Madsen, D. Kvasnicka and J. Luitz, *WIEN2k: An Augmented Plane Wave Plus Local Orbitals Program for Calculating Crystal Properties*, Institute of Physical and Theoretical Chemistry, TU Vienna, 2001.

24 J. P. Perdew, K. Burke and M. Ernzerhof, Generalized gradient approximation made simple, *Phys. Rev. Lett.*, 1996, **77**, 3865–3868.

25 F. Tran and P. Blaha, Accurate band gaps of semiconductors and insulators with a semilocal exchange-correlation potential, *Phys. Rev. Lett.*, 2009, **102**, 226401.

26 D. Koller, F. Tran and P. Blaha, Merits and limits of the modified Becke-Johnson exchange potential, *Phys. Rev. B: Condens. Matter Mater. Phys.*, 2011, **83**, 195134.

27 H. Schaefer, On the problem of polar intermetallic compounds: the stimulation of E. Zintl's work for the modern chemistry of intermetallics, *Ann. Rev. Mater. Sci.*, 1985, **15**, 1–41.

28 Y. Pei, X. Shi, A. D. Lalonde, H. Wang, L. Chen and G. J. Snyder, Convergence of bands for high thermoelectric performance, *Nature*, 2011, **473**, 66–69.

29 A. D. Lalonde, Y. Pei, H. Wang and G. J. Snyder, Lead telluride alloy thermoelectrics, *Mater. Today*, 2011, **14**, 526–532.

30 R. L. Petritz, Theory of photoconductivity in semiconductor films, *Phys. Rev.*, 1956, **104**, 15081516.

31 W. Zeier, A. Zevalkink, E. Schechtel, W. Tremel and G. J. Snyder, Thermoelectric properties of Zn-doped Ca_3AlSb_3, *J. Mater. Chem.*, 2012, **22**, 9826.

32 A. Zunger, Practical doping principles, *Appl. Phys. Lett.*, 2002, **83**, 57–59.

33 Y. I. Ravich, B. A. Efimova and I. A. Smirnov, *Semiconducting lead chalcogenides*, Plenum, New York, 1970.

34 H. J. Goldsmid and J. W. Sharp, *J. Electron. Mater.*, 1999, **28**, 869.

35 D. G. Cahill, S. K. Watson and R. O. Pohl, Lower limit to thermal conductivity of disordered crystals, *Phys. Rev. B: Condens. Matter Mater. Phys.*, 1992, **46**, 6131–6140.

36 D. G. Cahill and R. O. Pohl, Lattice vibrations and heat transport in crystals and glasses, *Annu. Rev. Phys. Chem.*, 1988, **39**, 93–121.

37 A. Zevalkink, E. S. Toberer, T. Bleith, E. Flage-Larsen and G. J. Snyder, Improved carrier concentration control in Zn-doped $Ca_5Al_2Sb_6$, *J. Appl. Phys.*, 2011, **110**, 013721.

38 H. J. Goldsmid, *Applications of Thermoelectricity*, J. Wiley and Sons Inc., New York, 1960.

